Metals and Materials International (2020) 26:1270–1285
https://doi.org/10.1007/s12540-019-00467-0

Effect of Heat Treatment on Microstructure and Properties of FGH4096M Superalloy Processed by Selective Laser Melting

Zhibo Hao[1] · Tian Tian[1] · Shiqing Peng[1] · Changchun Ge[1] · Xinggang Li[2,3] · Chonglin Jia[4] · Chuan Guo[3] · Qiang Zhu[3]

Received: 31 July 2019 / Accepted: 11 September 2019 / Published online: 21 September 2019

Abstract
A self-designed nickel-based superalloy, designated as FGH4096M, was prepared by selective laser melting (SLM). Different heat treatments were performed to improve the mechanical properties of the SLM alloy through optimizing the microstructures and the features of γ′ precipitates. Compared with the as-deposited alloy, the columnar grains with dendritic structures and equiaxed structures were retained in the alloy after direct aging, but a large amount of tertiary γ′ phase precipitated, especially around the sub-grain boundaries, resulting in the highest tensile strength but the lowest elongation. During solid solution and aging treatment (SSA), the recovery and recrystallization occurring in the alloy facilitated the grains to be equiaxed with the increase of solution temperature. For lower solution temperature (below 1100 ℃), the secondary γ′ precipitates decreased with the increase of solution temperature, while the tertiary γ′ precipitates from the subsequent aging process gradually increased; for higher solution temperature over 1100 ℃, exceeding the complete dissolution temperature of the γ′ phase, only tertiary γ′ precipitates from the subsequent aging process were uniformly distributed in the alloy. After double solid solution (1170 ℃ + 1050 ℃) + aging heat treatment (DSSA), there were three sizes of γ′ precipitates in the alloy. In general, the SLM + SSA (1130 ℃) alloy obtained the best comprehensive properties, which could be related to the homogenized microstructures and the uniform and dense distribution of single sized tertiary γ′ precipitates in the alloy.

Keywords Selective laser melting · Nickel-based superalloy · Heat treatment · γ′ phase · Microstructure · Tensile

1 Introduction

Nickel-based powder metallurgy (PM) superalloy is the preferred material for manufacturing advanced aeroengines due to its advantages of homogeneous microstructure, free from macrosegregation and high alloying degree [1, 2]. The alloy, designated as FGH4096, is the second generation damage-tolerant nickel-based PM superalloys, and has been widely used for its excellent high temperature strength and crack propagation resistance [3–5].

The selective laser melting (SLM) technique is regarded as one of the most promising additive manufacturing technologies [6]. Compared with the traditional technologies, the SLM shortens the production process of parts and components, especially during the R&D process of new products, thereby greatly improving the production efficiency; it also improves the material utilization ratio significantly [7]. The SLM can achieve near-net shape all at once and allows the rapid manufacturing of complex shape parts in accordance with the design, free from limitations of tools and molds [8]. In addition, the SLM has a laser spot diameter on the

✉ Changchun Ge
ccge@mater.ustb.edu.cn

✉ Xinggang Li
xing-gangli@163.com

[1] School of Materials Science and Engineering, University of Science and Technology Beijing (USTB), Beijing 100083, China

[2] Academy for Advanced Interdisciplinary Studies, Southern University of Science and Technology (SUSTech), Shenzhen 518055, China

[3] Department of Mechanical and Energy Engineering, Southern University of Science and Technology (SUSTech), Shenzhen 518055, China

[4] Science and Technology on Advanced High Temperature Structural Materials Laboratory, Beijing Institute of Aeronautical Materials (BIAM), Beijing 100095, China

10^1–10^2 microm level, producing parts of uniform structure, fine grain, low segregation and high density. Therefore, the SLM technique becomes a hot spot among scholars and research institutes in aerospace field for the manufacture of superalloy materials.

The SLM has been well studied for the nickel-based superalloys. Wang et al. [9] studied the microstructure, phase transformation and mechanical properties of the SLM and SLM + HT Inconel 718, and they found that heat treatment (HT) was crucial for the improvement of mechanical properties. Holland et al. [10] performed multiscale characterization of microstructures and mechanical properties of the SLM and SLM + HT Inconel 718, and they found that HT reduced the wear rate, enhanced the hardness, removed the texture and randomized the grain orientation. Meanwhile, recrystallized grains and twins appeared in the SLM + HT Inconel 718. Divya et al. [11] analyzed the structure and precipitated phases of the SLM CM247LC in the deposited and HT states. They found that the dislocations in the deposited state alloy were mainly distributed on the sub-grain boundaries, and there was large residual stress inside the alloy. They also discussed the effect of HT on γ′ precipitation, which could have a great impact on mechanical properties. Yao et al. [12] investigated the effects of HT on microstructures and tensile properties of pure IN718 and IN718/TiC nanocomposite fabricated by SLM. They found that in both pure IN718 and IN718/TiC nanocomposite, heat treatment dissolved the brittle Laves phase and promoted the precipitation of strengthening γ′/γ″, δ, and MC/$M_{23}C_6$ carbides from the γ matrix. Therefore, heat treatment improved the tensile strength but decreased the ductility of both pure IN718 and IN718/TiC nanocomposite. A novel heat treatment including higher temperature homogenization at 1150 °C for 2 h and one-time lower temperature aging treatment at 700 °C for 12 h was performed on the SLM Inconel 718 alloy by Li [13], which can overcome the strength-plasticity tradeoff of Inconel 718 alloy. The results showed that recrystallized grains with annealing twins and ultrafine strengthening phases formed in the specimen subjected to the novel heat treatment, which improved plasticity by 41% and maintained ultimate strength at the same level achieved by the traditional heat treatment. Zhang et al. [14] revealed the effect of heat treatment on the microstructural evolution of the SLM Inconel 625 through in-situ synchrotron X-ray scattering and diffraction, demonstrating that the homogenization heat treatment can homogenize the SLM alloy. Huang et al. [15] prepared K4202 nickel-based superalloy by SLM, and studied the structure and mechanical properties of the alloy after deposition and HT, reporting better room temperature properties in the SLM + HT state than in the casting state.

Despite a great deal of research on the preparation of nickel-based superalloys by SLM, there are few studies on the preparation of nickel-based PM superalloys by SLM. Based on the previous studies, it can be concluded that heat treatment (HT) is an important and essential post-treating process for the SLM nickel-based superalloys. In this paper, based on the composition of FGH4096 PM superalloy, a new type FGH4096M superalloy was designed by adding trace Mg element. The microstructure and properties of the SLM and SLM + HT FGH4096M were studied in detail, so as to provide some technical reference for the SLM nickel-based PM superalloys.

FGH4096M is a kind of precipitation hardening alloy and the γ′ precipitate is the main strengthening phase [16, 17]. The properties of the alloy depend on the amount, size, shape and distribution of γ′ precipitate and heat treatment (HT) directly affects these factors above [18–20], so a suitable HT system can effectively improve the mechanical properties. In addition, the solid solution treatment has a significant impact on the grain microstructure. Therefore, heat treatment is a key factor to improve the overall performance of the alloy.

2 Materials and Methods

As a starting process, FGH4096M prealloyed powder was prepared through gas atomization, with an average size of about 25 μm and chemical composition of 0.033%C–15.84%Cr–13.3%Co–4.08%W–4.12%Mo–2.26%Al–3.79%Ti–0.78%Nb-minZr-minB-minMg-bal. Ni (mass fraction, wt%). The surface morphology of the prealloyed powder is shown in Fig. 1.

The FGH4096M alloy was produced during the SLM process on an equipment of Concept Laser Company, which had a single-mode fiber laser, a maximum power of 95 W, a spot diameter of 45 μm, a maximum laser scanning speed of 7000 mm/s and a forming space of 90 mm × 90 mm × 80 mm. Argon (Ar) was used as shielding gas to keep the oxygen content below 100 ppm in the forming space. The laser power was 95 W and the

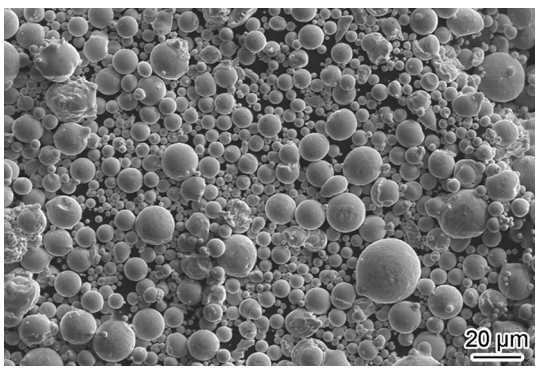

Fig. 1 Morphology of FGH4096M alloy powder

successive adjacent layers were scanned with a rotating angle of 90°, a speed of 1300 mm/s and a hatch distance of 30 μm. The powder layer thickness was 25 μm. These SLM process parameters have been optimized in another work [21]. The specimens in dimensions of 10 mm × 10 mm × 10 mm for microstructure observation and the specimens in dimensions of 25 mm × 4 mm × 2 mm for tensile test were prepared during the SLM process according to Chinese GB/T 228–2002 standard. The average values of tensile properties, such as ultimate strength (σ_b), yield strength ($\sigma_{p0.2}$) and elongation (δ), based on at least three specimens were collected during the tensile tests. The loading direction of the tensile test sample was the same as the deposition direction (z-axis) of the as-built test sample.

Three kinds of heat treatments (HTs) were carried out to the SLM specimens: direct aging (DA), solid solution + aging (SSA) and double solid solution + aging heat treatments (DSSA). The DA treatment was carried out, holding 20 h at a temperature of 760 °C, followed by air cooling. During the SSA treatment, the solid solution treatment was performed at the solution temperature of 1010 ℃, 1030 ℃, 1050 ℃, 1070 ℃, 1090 ℃, 1110 ℃, 1130 ℃ and 1150 ℃, respectively, holding 4 h before water quenching. During the DSSA treatment, the specimens were firstly kept at the solution temperature of 1170 ℃ for 4 h, subsequently water-quenched, then kept at 1050 ℃ for 4 h, and finally water-quenched. The specimens with different solid solution treatments were subjected to insulation for 20 h at a temperature of 760 °C, followed by air cooling. The schematics for three kinds of HTs were shown in Fig. 2.

The microstructures and properties of the SLM and the SLM + HT alloys were characterized. After being ground, polished and etched with (10 g $CuCl_2$ + 100 ml HCl + 100 ml C_2H_5OH) reagent, all the specimens were observed under an optical microscope XTX-200 of Jiangnan Optical Instrument Factory. After being ground, polished, electropolished for 45 s in (20 vol% H_2SO_4 + 80 vol% CH_3OH) reagent with a 30 V DC power, and etched electrolytically for 10 s in (9 g CrO_3 + 90 ml H_3PO_4 + 30 ml CH_5OH) reagent with a 5 V DC power, all the specimens were observed through the JSM-6701F field emission scanning electron microscope (SEM) to reveal their morphology. The phases were examined through the equipped energy dispersive spectrometer (EDS). The crystallographic information of grains was detected by an electron backscatter diffraction (EBSD) system with a step size of 1 μm and the data were analyzed using Oxford HKL Channel 5 software. The tensile tests were performed on an equipment model WDW200D by Jinan Time Shijin Testing Machine Group Co. Ltd, with a strain rate of 10^{-3}/s.

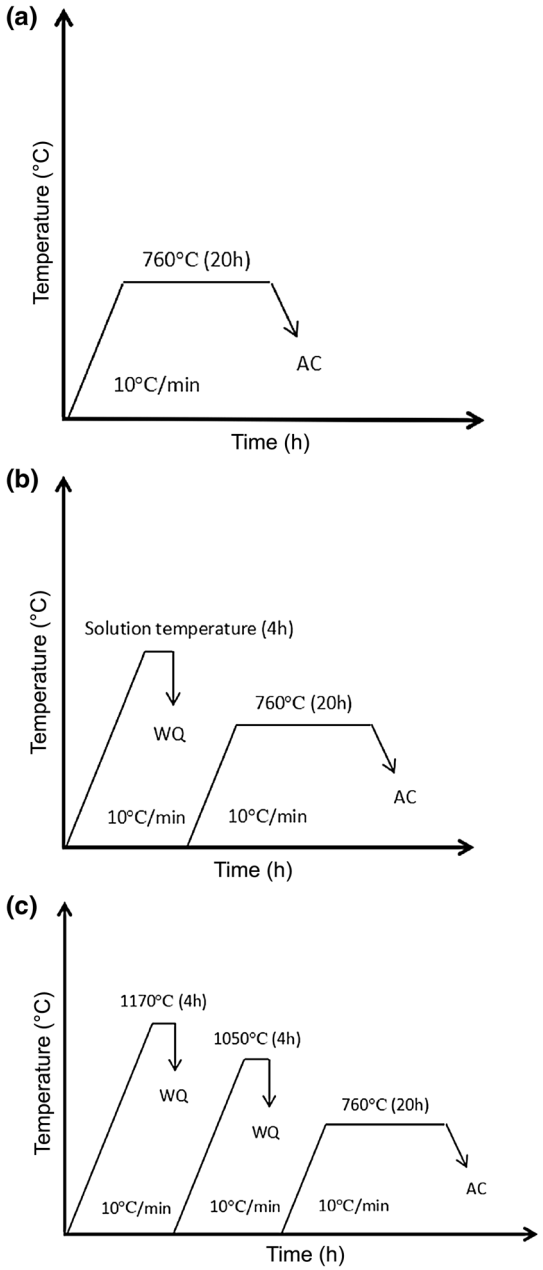

Fig. 2 Schematics of different heat treatments for SLM FGH100L: **a** direct aging, **b** solid solution + aging, **c** double solid solution + aging. *AC* air cooling, *WQ* water quenching

3 Results

3.1 Microstructure of SLM FGH4096M

Figure 3 shows the metallographic microstructure of the SLM alloy, indicating a good metallurgical bonding. The microstructures in the vertical plane are shown in Fig. 3a, from which it can be seen that the thickness of the molten pool is 25–30 μm and the alloy is mainly composed of columnar grains growing across multiple layers and

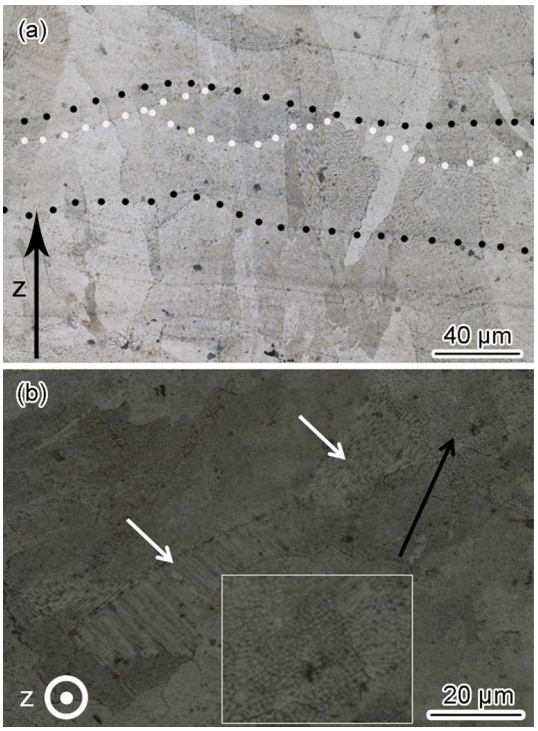

Fig. 3 **a** Microstructure of SLM FGH4096M: vertical plane, **b** horizontal plane, z-axis indicating the building direction

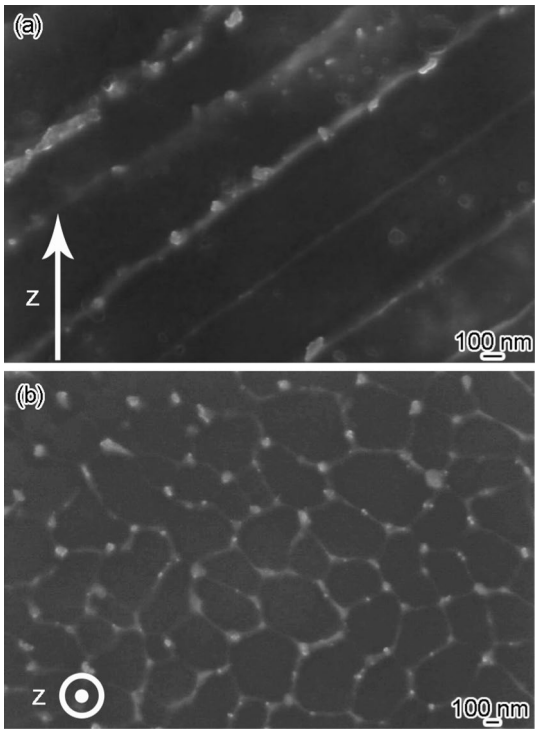

Fig. 4 SEM morphology of SLM FGH4096M: **a** vertical plane, **b** horizontal plane, z-axis indicating the building direction

basically along the forming direction. These columnar grains with varying contrast and width from a dozen to dozens of microns had flat grain boundaries generally. Some columnar grains with a small length were confined to the molten pool. The dendritic structures with a size of about 0.5 μm were arranged in the columnar grains, similar to the directional solidification or casting microstructures [9, 22]. The growth direction of the dendritic structures was consistent with that of columnar grains. The scanning strategy with a rotating angle 90° between the adjacent layers led to the molten pool tracks as shown in Fig. 3a (the white dotted line was the cross section of the molten pool, while the black dotted line was the longitudinal section of the molten pool). The powder layer scanned by laser was melted completely, while the former solidified layer was melted partially again. Because the large temperature gradient and high storage energy in the SLM alloy resulted from the high cooling rate [21], it is not a good condition for the formation of new grain nuclei. Hence, the grains grow preferentially on the previously solidified grains, forming dendritic structures and equiaxed structures.

Figure 3b shows the microstructure in the horizontal plane of the SLM alloy, in which the orthogonal molten pool tracks again revealed the laser scanning strategy for the adjacent layers to rotate 90°. The grains exhibited irregular shapes in the horizontal plane. Most of grains were confined to the molten pool with an average width of about 35 μm, while some grains extended to other pools. This was affected by the heat source induced by laser movement. No large precipitates were observed at the grain boundary. Although the equiaxed cellular structures were dominant in many grains (as shown in the embedding figure in Fig. 3b), there were dendritic structures parallel to the cross section in some grains (indicated by the white arrow), indicating that a small amount of heat flow transversely transferred to the molten pool boundary after powder molten.

Figure 4 shows the SEM morphology of the dendritic structures and cellular structures in the SLM alloy. There were fine precipitates in the form of MC carbide at the boundary of the dendritic structures and cellular structures [22], and the size of MC was below 100 nm. Figure 4a is the SEM morphology on the vertical plane parallel to the forming direction. A large number of carbides were precipitated at the boundary of the dendritic structure. A few near-spherical precipitates in the dendritic structure were fine γ′ strengthening particles with a size below 100 nm [11]. Due to the high cooling rate, the γ′ phase precipitated in a small amount and size. Figure 4b shows the SEM morphology on the horizontal plane vertical to the forming direction. The fine MC carbides precipitated at the boundary of cellular structure. Most of large MC carbides in a size range of 50–100 nm precipitated at the intersection of different boundaries of equiaxed structures, while small MC carbides

with a size below 50 nm tended to precipitate at the boundary of two adjacent equiaxed structures.

3.2 Microstructure of SLM + HT FGH4096M

3.2.1 Metallographic Microstructure of SLM + HT FGH4096M

The SLM alloy was treated by DA, SAA and DSSA to understand the evolution of the microstructure during the experimental process. Figures 5–7 show the microstructures of the SLM + HT alloys.

Figure 5a shows the vertical plane morphology of the SLM + DA alloy. It basically maintained the microstructure of columnar grains across multiple layers as in the SLM deposited alloy. There were still relatively fine dendritic structures or equiaxed structures inside columnar grains (as shown in the embedded figure). Figure 5b shows the horizontal plane morphology of the SLM + DA alloy. The molten pool trace inherited from the SLM alloy was blurred after DA. Compared with the SLM alloy, the grain morphology in the SLM + DA alloy changed little, and the dendritic and cellular structures were retained in the grains (as shown in the embedded figure).

Figure 6a shows the vertical plane morphology of the SLM + SSA (1050 ℃) alloy. The alloy still maintained the dendritic structures and equiaxed structures within columnar grains, but some of the columnar grain boundaries began to bend (as indicated by the white arrow in Fig. 6a). Simultaneously, there were more precipitates at the boundaries of the columnar grains, dendritic structures and cellular structures. Figure 6b shows the horizontal plane morphology of the SLM + SSA (1050 ℃) alloy. The grains with irregular shapes in the alloy were confined to the areas arranged regularly like checkerboard. In each grid, there were one bigger grain in the center and a few smaller grains at the edge. And the boundaries of grains at the edge of grid began to protrude, as shown in the embedded figure in Fig. 6b. There were more precipitates at the boundaries of the columnar grains, dendritic structures and cellular structures. Compared with the SLM + SSA (1050 ℃) alloy, the metallographic microstructures in the SLM + SSA (1070 ℃) and SLM + SSA (1090 ℃) alloys changed little, so no pictures are shown here for them.

Figure 6c, d show the morphology of the SLM + SSA (1100 ℃) alloy. It could be concluded that the microstructure of the alloy at the solution temperature over 1100 °C began to change significantly compared with that at the lower solution temperature. The main reason was that the SLM alloy with a high cooling rate had a high temperature gradient, eventually leading to high storage energy inside [23, 24]. When the solution temperature was increased to 1110 °C, reaching the recovery and static recrystallization temperature of the alloy, the higher storage energy acted as the driving force to promote the recovery and recrystallization process. At the same time, the rapid migration of columnar grain boundaries and the rapid diffusion of alloying elements accelerated the disappearance of dendritic structures and cellular structures [23–27]. Therefore, the microstructure of the alloy changed greatly under this condition. Figure 6c shows the vertical plane morphology of the SLM + SSA (1110 °C) alloy. The columnar grain boundaries underwent a significant migration process along the short axis direction, and protruded largely. As the holding time increased, the grain boundaries continued to migrate and connected with the sub-adjacent grains, thereby shortening the length of adjacent grains in the deposition direction [25]. Twins could be observed in Fig. 6c due to the high content of Co in the alloy, which lowered the stacking fault energy. The dislocation slip of the alloy was hindered to form twins [28, 29]. Figure 6d shows the horizontal plane morphology of the SLM + SSA (1110 °C) alloy. Due to the occurrence of recovery and recrystallization and the migration of grain boundaries, the checkerboard-like distribution of grains in the alloy gradually disappeared, and the grain boundaries inside the checkerboard were bent outwardly and migrated. During this process, the grains on the checkerboard edge deformed due to bend. Further, fine grains formed, and some of them even split into finer grains (as shown in the white dotted frame of Fig. 6d). The high storage energy in the

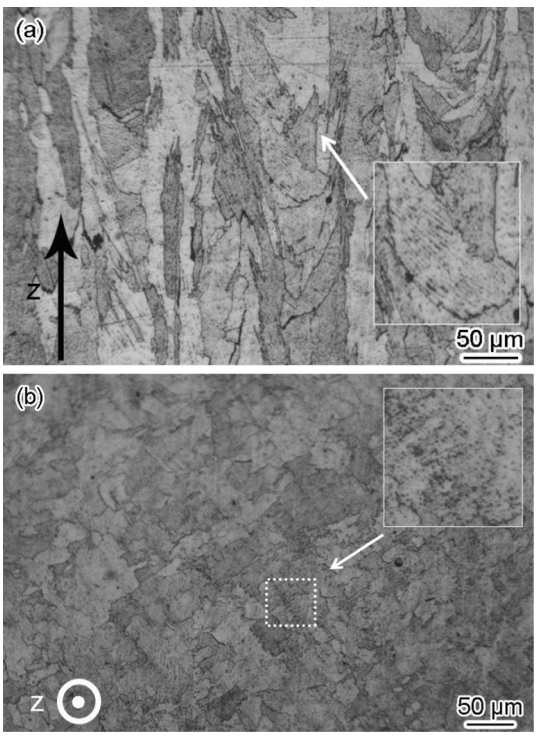

Fig. 5 Microstructure of SLM + DA FGH4096M: **a** vertical, **b** horizontal, z-axis indicating the building direction

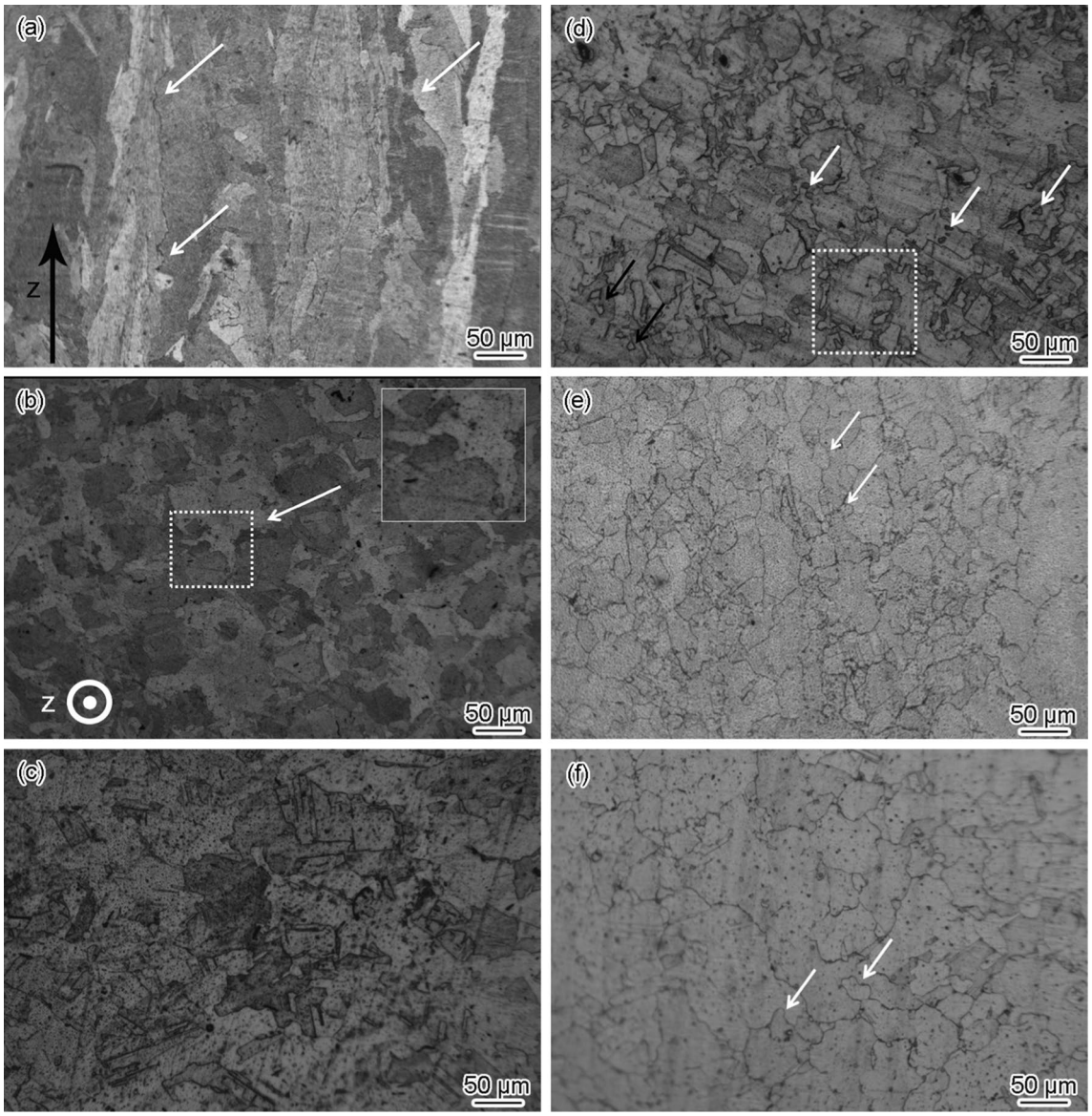

Fig. 6 Metallographic microstructure of SLM + SSA FGH4096M: **a** SSA (1050 ℃), vertical; **b** SSA (1050 ℃), horizontal; **c** SSA (1100 ℃), vertical; **d** SSA (1100 ℃), horizontal; **e** SSA (1130 ℃), vertical; **f** SSA (1130 ℃), horizontal. z-axis indicating the building direction

SLM alloy made it easier to form recrystallized grains at the checkerboard boundary (indicated by the white arrow in Fig. 6d). The formation and growth of the recrystallized grains were also factors that promoted the disappearance of the chekerboard-like grain distribution phenomenon. There were also a few recrystallized grains at the checkerboard center (as indicated by the black arrow in Fig. 6d). The appearance of twins as shown in Fig. 6d had an influence on the morphology of grains. In general, the dendritic structures and equiaxed cellular structures in the grains disappeared under SSA (1110 °C).

As the solution temperature increased, the rate of atomic diffusion and grain boundary migration continued to increase, and the static recrystallization became more sufficient. The columnar grain boundaries migrated along the short axis direction, and the columnar grains were transformed to equiaxed grains. The number of equiaxed grains increased, and the grain growth was accelerated. Figure 6e shows the vertical plane morphology of the SLM + SSA (1130 °C) alloy. The grains were irregularly polygonal and tended to be equiaxed. Due to the migration of the columnar grain boundary, the grain size was shortened in the vertical direction, which played a role in refining the grain. Some of the recrystallized grains at the boundary of columnar grains began to grow (as indicated by the white arrow in Fig. 6e). Figure 6f shows the

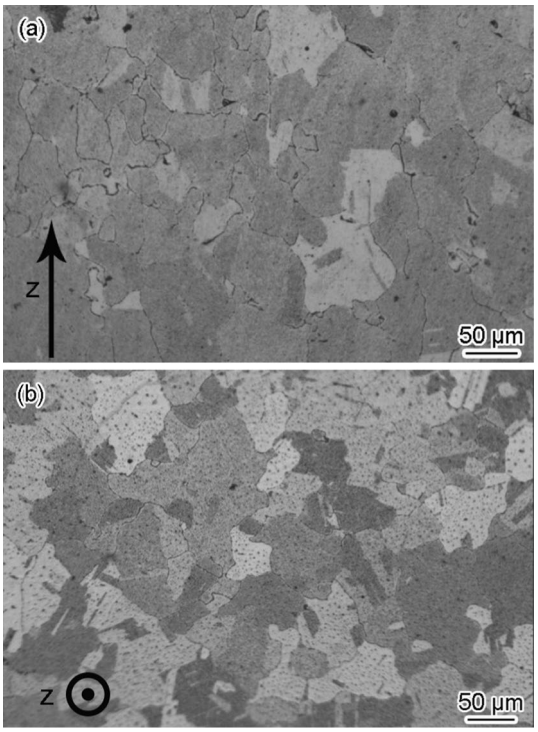

Fig. 7 Microstructure of SLM + DSSA (1170 ℃ + 1050 ℃) FGH4096M: **a** vertical, **b** horizontal, z-axis indicating the building direction

horizontal plane morphology of the SLM + SSA (1130 °C) alloy. Many grain boundaries in the alloy were curved, and some of them extended toward the inside of adjacent grains (as indicated by the white arrow in Fig. 6f). A large number of recrystallized grains with a wide size range in the alloy indicated that some recrystallized grains started to grow. Most of the recrystallized grains were distributed at the original grain boundaries and a small number of twins were present in the alloy. With the continuous increase of solution temperature, the recrystallization process in the alloy was basically completed, e.g., in the cases of SLM + SSA (1150 °C) and SLM + SSA (1170 °C), but the grains barely grew.

Figure 7a, b show the metallographic morphology of the SLM + DSSA (1170 °C + 1050 °C) alloy. As shown in Fig. 7a, on the vertical plane of the alloy, the recrystallization process had been basically completed, followed by grain growth. The grains with irregular shapes and different sizes exhibited slightly curved grain boundaries. Figure 7b shows the microstructure of the alloy in the horizontal plane. The grains were still in irregular polygonal shapes, and the grain boundaries were curved after the double-solution treatment of the alloy. Some twins and many fine precipitates could be observed in the grains under the optical microscope.

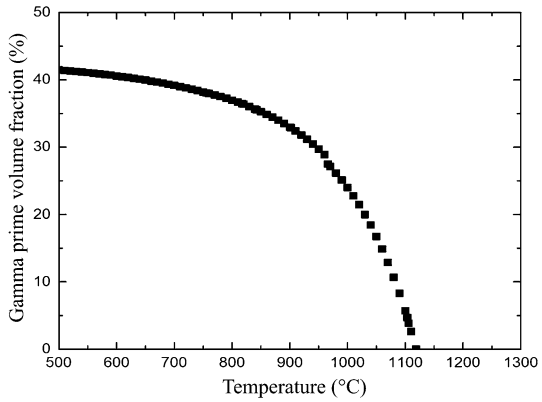

Fig. 8 The relationship between the volume fraction of γ′ precipitate and the precipitation temperature calculated by Jmatpro

3.2.2 Morphology of γ′ Phase in SLM + HT FGH4096M

Not only the grain size but also the precipitation behavior of strengthening phase are very sensitive to the HT systems for the SLM alloy. The γ′ phase is the main strengthening phase of the FGH4096M alloy and the amount, size and distribution of γ′ precipitate have a great impact on the properties of the alloy [28–31]. Therefore, it is of great significance to study the effect of the HT system on the precipitation behavior of γ′ phase. The relationship between the amount of γ′ precipitate and the precipitation temperature was calculated by Jmatpro, as shown in Fig. 8, which indicated that the amount of precipitated γ′ phase gradually decreased with the temperature increasing and began to decrease dramatically above 1000 °C. The γ′ phase totally disappeared at the solution temperature of 1120 °C. Combined with the analysis of Jamatpro software, the precipitation behavior of γ′ phase during DA, SSA and DSSA was investigated, respectively.

Figure 9a, b show the SEM photographs of the SLM + DA alloy. Since the SLM alloy did not recover and recrystallize at a relatively lower aging temperature, the metallographic microstructure of columnar grains was basically maintained, as in the initial SLM state. After the DA treatment, a large number of nearly spherical tertiary γ′ precipitates with an average size of 32.8 nm were formed in the dendritic structures and cellular structures, and especially at the grain boundaries. Figure 9a shows the γ′ morphology in the vertical plane of the SLM + DA alloy. Because the γ′ phase forming elements segregated at the boundary of the dendritic structure, the amount of γ′ precipitate at the boundary was larger than that inside, and the boundary of the dendritic structure coarsened. Figure 9b shows the γ′ phase morphology in the horizontal plane of the SLM + DA alloy. The size and shape of the γ′ precipitate in the horizontal plane were the same as in the vertical plane, and there were more γ′ precipitates at the boundary of cell structures.

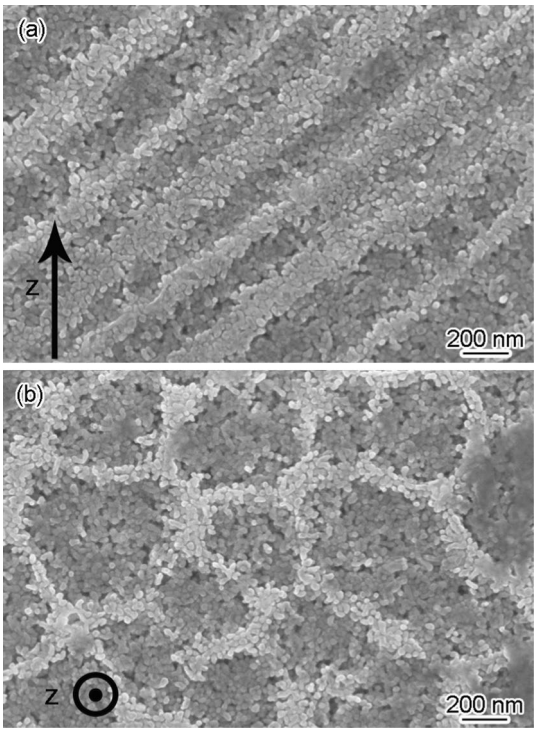

Fig. 9 SEM images of microstructure and morphology of γ′ precipitates in SLM + DA FGH4096M: **a** vertical, **b** horizontal, z-axis indicating the building direction

The relatively higher cooling rate led to high concentration vacancies inside the alloy and high density dislocations at the boundaries of the dendritic structure and the cellular structure during the SLM process [11, 32, 33]. In the subsequent HT process, the strengthening elements, such as Al and Ti, were more easily to interchange with the vacancies, thereby promoting the nucleation and growth of the γ′ phase [31, 34]. Meanwhile, the atoms were irregularly arranged at the boundaries of the columnar grain, dendritic structure and equiaxed structure, where the atomic mixing entropy was high and more diffusion channels promoted the diffusion of strengthening elements, lowering the energy barrier for the precipitation of the γ′ phase [31]. During the DA process, the strengthening elements such as Al and Ti diffused slowly in a relatively low temperature, so the γ′ precipitates preferentially nucleated near vacancies and dislocations, or at the boundaries of dendritic structures and cellular structures. The fine γ′ precipitates grew by absorbing Al and Ti elements nearby. But the growth rate of all the γ′ precipitates in the alloy was so slow that the γ′ precipitates dispersed inside the alloy. At the same time, the boundaries of columnar grain, dendritic structure and cellular structure did not migrate significantly. There were a large number of dislocations at the boundaries of dendritic structure and equiaxed structure, which was beneficial to the precipitation of the γ′ phase. Thus the γ′ phase precipitated more at the boundaries of dendritic structure and cellular structure than that in the interior (as shown in Fig. 9a and b).

Figure 10a shows the SEM images of γ′ precipitates in the SLM + SAA (1010 °C) alloy. The secondary γ′ precipitates, with square or nearly spherical shapes and an average size of about 250 nm, were arranged along the direction of the dendritic structure. A small number of nearly-spherical tertiary γ′ precipitates with a size of about 30 nm were distributed between the secondary γ′ precipitates (as shown in the embedded figure in Fig. 10a). Although the diffusion rate of the strengthening elements in the alloy increased at the solution temperature of 1010 °C, the recovery process was relatively slow at this temperature. So more strengthening elements in the alloy were concentrated at the boundaries of the grain, dendritic structure and cellular structure. At this point, the overall fraction of the γ′ phase in the alloy decreased as shown in Fig. 8, but the rapid diffusion of the strengthening elements promoted secondary γ′ to precipitate and grow rapidly with larger sizes at the boundaries of the dendritic structures and the cellular structures. The black dotted line in Fig. 10a represented the columnar grain boundary, where the distribution of the secondary γ′ precipitates was irregular compared with that in the interior of the columnar grains. This mainly resulted from the different orientations of columnar grains and dendritic structures. In addition, the atoms at the grain boundary were irregularly arranged, so that the precipitation of the γ′ phase was relatively irregular. It was also observed that some γ′ precipitates began to combine to form larger γ′ precipitates, as shown by the circle in Fig. 10a.

Figure 10b shows the SEM images of γ′ precipitates in the SLM + SSA (1030 °C) alloy. The number of secondary γ′ precipitates in the alloy under the solution temperature 1030 °C significantly reduced compared with that under 1010 °C. This agrees with the conclusion in Fig. 8, i.e., the amount of γ′ phase in the alloy decreased with the increase of solution temperature. As shown in Fig. 10b, the γ′ precipitates in the interior of columnar grains were still regularly arranged along the direction of the dendritic structures. The increase of solution temperature promoted the diffusion of strengthening elements and the recovery process in the alloy. However, at this temperature, the diffusion of strengthening elements was still dominant, and the diffusion channels were less than that at 1010 °C, so the average size of the secondary γ′ precipitates was relatively large, about 309 nm. In the meantime, the adjacent secondary γ′ precipitates segregated at the boundary of the dendritic structure appeared to fuse to a large extent, as shown in the dotted ellipse in Fig. 10b. The secondary γ′ precipitates with different orientations, represented by the dotted lines in Fig. 10b, were arranged at both sides of the grain boundaries, and the primary γ′ precipitates with large size and irregular shape were formed by the combination of multiple secondary γ′ precipitates at

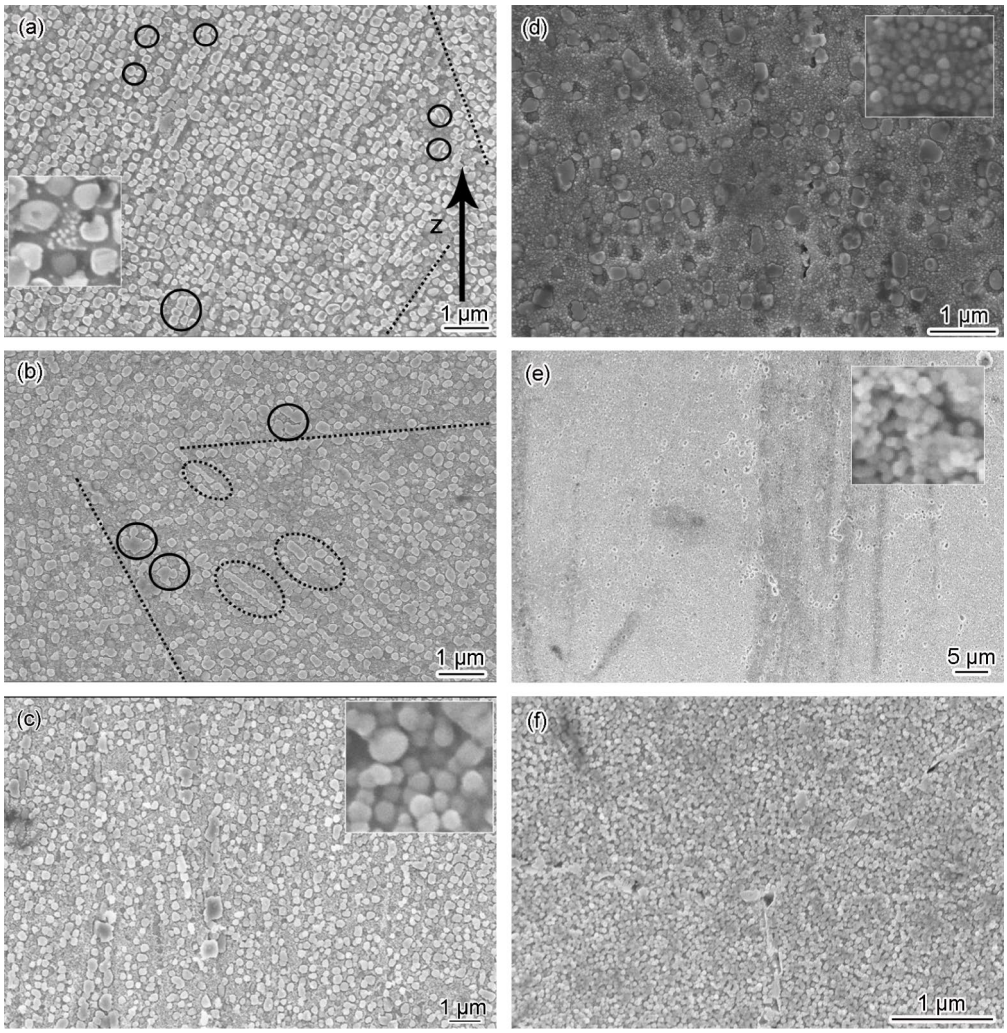

Fig. 10 SEM images of microstructure and morphology of γ′ precipitates in SLM + SSA FGH4096M: **a** SSA (1010 ℃), vertical; **b** SSA (1030 ℃), vertical; **c** SSA (1050 ℃), vertical; **d** SSA (1070 ℃), vertical; **e** SSA (1090 ℃), vertical; **f** SSA (1110 ℃), vertical. z-axis indicating the building direction

the grain boundary as shown by the black circle in Fig. 10b. The combination of the secondary γ′ precipitates was mainly driven by the reduction of the interface energy. Due to the increase of the solution temperature, the matrix absorbed much more strengthening elements, so that many tertiary γ′ particles precipitated in the interior of grains during the subsequent aging process.

Figure 10c shows the SEM images of γ′ precipitates in the SLM + SSA (1050 °C) alloy. The cubic primary γ′ particles with sizes from 400 to 500 nm were precipitated at the grain boundaries after solid solution treatment at 1050 °C. The size of the secondary γ′ precipitates increased slightly, but the number decreased compared with that in the SLM + SSA (1030 °C) alloy, which was consistent with the calculated results in Fig. 8. Most of these secondary γ′ precipitates were distributed along the direction of the dendritic structures in the grains. The larger secondary γ′ precipitates were cubic, while the smaller secondary γ′ precipitates were spherical. More strengthening elements dissolved in the matrix, and the recovery process in the alloy was accelerated with the increase of solution temperature. Although the diffusion rate of strengthening elements increased, the combination phenomenon of secondary γ′ precipitates was rarely observed. A large number of alloying elements dissolving in the alloy matrix precipitated in the form of tertiary γ′ phase during the subsequent aging process (as shown in the embedding diagram in Fig. 10c).

Figure 10d shows the SEM images of γ′ precipitates in the SLM + SSA (1070 °C) alloy. The precipitation of secondary γ′ phase decreased significantly after solid solution treatment at 1070 °C. Due to the large quantity of alloy strengthening elements dissolving in the matrix and the rapid recovery process in the alloy, most of secondary and tertiary γ′ precipitates were randomly distributed with only a small number of

secondary γ′ precipitates still maintaining the arrangement along the direction of the dendritic structures. The size of secondary γ′ precipitates at the grain boundary was about 222 nm, close to those in the interior of grains.

Figure 10e shows the SEM images of γ′ precipitates in the SLM + SSA (1090 °C) alloy. Only very few secondary γ′ precipitates were distributed at the grain boundary of the alloy, while a large number of tertiary γ′ precipitates were dispersed in the interior of grains. According to the calculated results in Fig. 8, the precipitation of secondary γ′ phase was about 8.3% in the equilibrium state at a solution temperature of 1090 °C (as shown in Fig. 8), which was consistent with that shown in Fig. 10e.

Figure 10f shows the SEM images of γ′ precipitates in the SLM + SSA (1110 °C) alloy. In this case, the solution temperature was close to the complete solution temperature of the γ′ phase, and great changes of the microstructure in the alloy resulted from the rapid static recovery process, static recrystallization and rapid grain boundary migration. The alloy was in a supersaturated state, and the alloy elements were uniformly dissolved in the matrix. Under the subsequent aging process, the tertiary γ′ particles with an average size of 33.1 nm precipitated uniformly inside the grain. There were nearly no primary γ′ precipitates and secondary γ′ precipitates at the grain boundary or in the grain. As the solid solution temperature continued to rise, exceeding the complete solution temperature of the γ′ phase, the morphology of the γ′ precipitates formed during the subsequent aging process was similar to that in the SLM + SSA (1110 °C) alloy.

Figure 11a shows the SEM images of γ′ precipitates in the SLM + DSSA (1170 °C + 1050 °C) alloy. It could be seen that the γ′ precipitates with three sizes were distributed in the alloy. The primary γ′ precipitates with the size between 0.8 and 1 μm in cubic or irregular shapes were distributed at the grain boundary; the secondary γ′ precipitates were distributed in the gains with the size between 400 and 500 nm in cubic shape; the tertiary γ′ precipitates were distributed in the gaps between primary γ′ precipitates and secondary γ′ precipitates, with the larger size between 100 and 150 nm mostly in cubic, bell or petal-like shapes, and the smaller size of several tens nanometers in spherical shape. The alloy undergoing the first solid solution treatment at 1170 °C was in a super-solid solution state, and the solid solution elements were uniformly distributed in the matrix. Some defects remaining inside the alloy after solid solution treatment at 1170 °C resulted from many vacancies and dislocations inside the SLM alloy with rapid solidification. When the alloy underwent a second solution treatment at 1050 °C, the strengthen elements diffused rapidly in a sub-solid solution alloy and preferentially segregated to form primary γ′ precipitates at the grain boundary with a low energy barrier. During the middle and latter stages of the solid solution

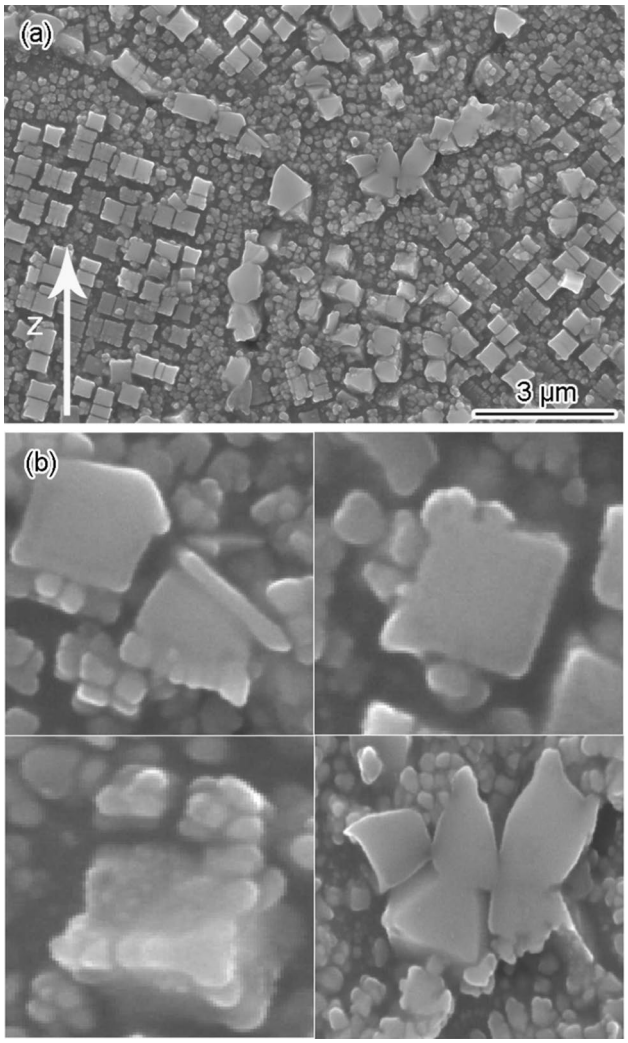

Fig. 11 SEM images of microstructure and morphology of γ′ precipitates in SLM + DSSA FGH4096M: **a** DSSA (1170 ℃ + 1050 ℃), vertical, z-axis indicating the building direction; **b** fusion and growth of γ′ precipitates

treatment, the alloy elements were segregated in the vicinity of vacancies and dislocations to form secondary γ′ precipitates. Later, a few tertiary γ′ precipitates began to nucleate. During the aging process, the sizes of the primary and secondary γ′ precipitates increased, and the earlier nucleated tertiary γ′ precipitates began to grow. Meanwhile, there were also small sized tertiary γ′ precipitates, which had little time to grow. In the second solid solution process at 1050 °C, the growth of primary and secondary γ′ precipitates mainly depended on the diffusion and segregation of strengthening elements. During the last stage of aging process, with the growth of the larger tertiary γ′ precipitates and the nucleation of smaller tertiary γ′ precipitates, the contents of the strengthening elements in the matrix became very low. In this case, a large number of secondary and tertiary γ′ precipitates led to high interface energy in the alloy. In order

to reduce the interfacial energy, the primary and secondary γ′ precipitates began to absorb the tertiary γ′ precipitates around them for fusion and growth, as shown in Fig. 11b.

The average sizes of γ′ precipitates, including primary γ′, secondary γ′ and tertiary γ′, in the alloys under different HTs were measured by the ImageJ software, as shown in Fig. 12. The average sizes of γ′ in the SSA (1050 °C) and DSSA (1170 °C + 1050 °C) alloys were relatively larger, about 197 nm and 208 nm, respectively; while the average sizes of γ′ in the DA and SSA (1130 °C) alloys were relatively smaller, about 32.8 nm and 33.1 nm, respectively.

3.3 Mechanical properties of SLM FGH4096M and SLM + HT FGH4096M

The room temperature tensile and hardness tests were carried out on the SLM and SLM + HT alloys. The loading direction of the specimen was parallel to the deposition direction (z-axis). The tensile curves are shown in Fig. 13a. As shown in the figure, the SLM FGH4096M had a high elongation at room temperature, but its tensile strength was low. After HT, the tensile strength of the alloy increased. In particular, the strength of the alloy increased significantly after DA treatment, but the elongation was decreased. Figure 13b shows the hardness values of the alloys under different treatment conditions. The hardness values of the alloys after DA and SSA (1130 °C) treatments were relatively high, 448.87HB and 429.56HB, respectively.

Table 1 shows the room temperature tensile properties (average values) of the SLM alloy and the SLM + HT alloy. The SLM + DA alloy had the highest room temperature ultimate strength (1595.56 MPa) and yield strength (1459.46 MPa), 32.51% and 52.31% higher than that of the SLM alloy, respectively. The room temperature tensile properties of the SLM + DA alloy had exceeded that of the as-forged alloy.

Considering the overall properties, the SLM + DA and SLM + SSA (1130 °C) alloys had the best comprehensive properties. There were only nano-sized tertiary γ′ precipitates in the alloys under these two treatments, so the fine

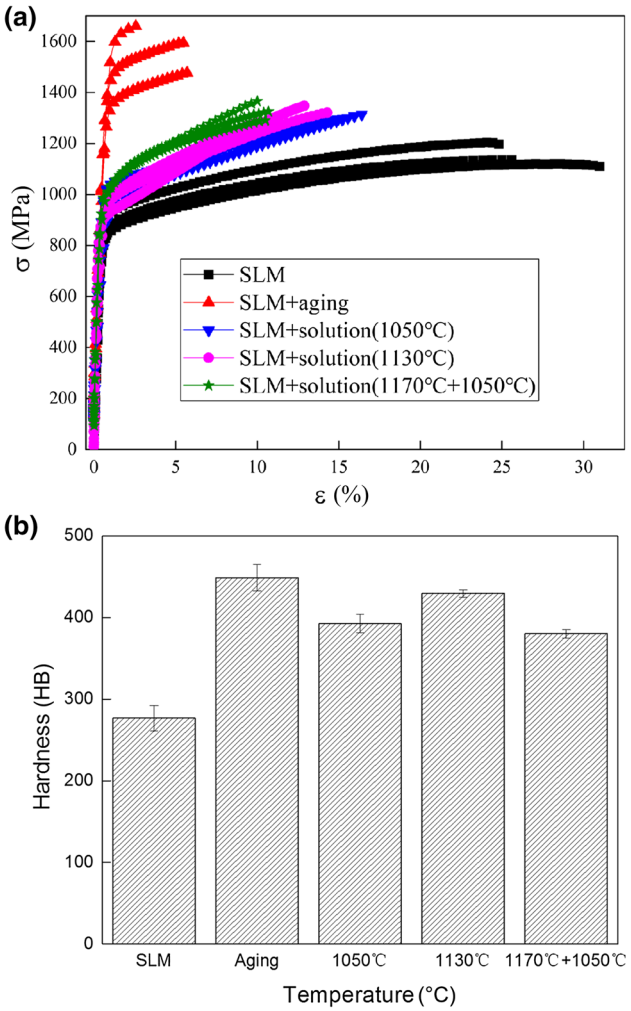

Fig. 13 Room temperature mechanical properties of SLM FGH4096M under different heat treatments: **a** tensile properties, **b** hardness

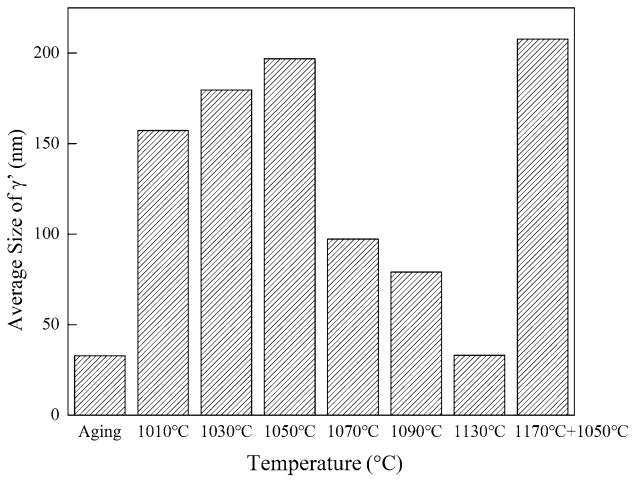

Fig.12 The average sizes of γ′ precipitates in SLM FGH4096M under different HTs

Table 1 Room temperature tensile properties (average values) of SLM FGH4096M under different heat treatments

	σ_b (MPa)	$\sigma_{p0.2}$ (MPa)	δ (%)
SLM	1204.13	958.22	24.97
SLM + DA	1595.56	1459.46	5.49
SLM + SSA (1050 ℃)	1299.75	1039.86	15.68
SLM + SSA (1130 ℃)	1322.02	1006.36	14.44
SLM + DSSA (1170 ℃ + 1050 ℃)	1325.72	1037.86	10.74

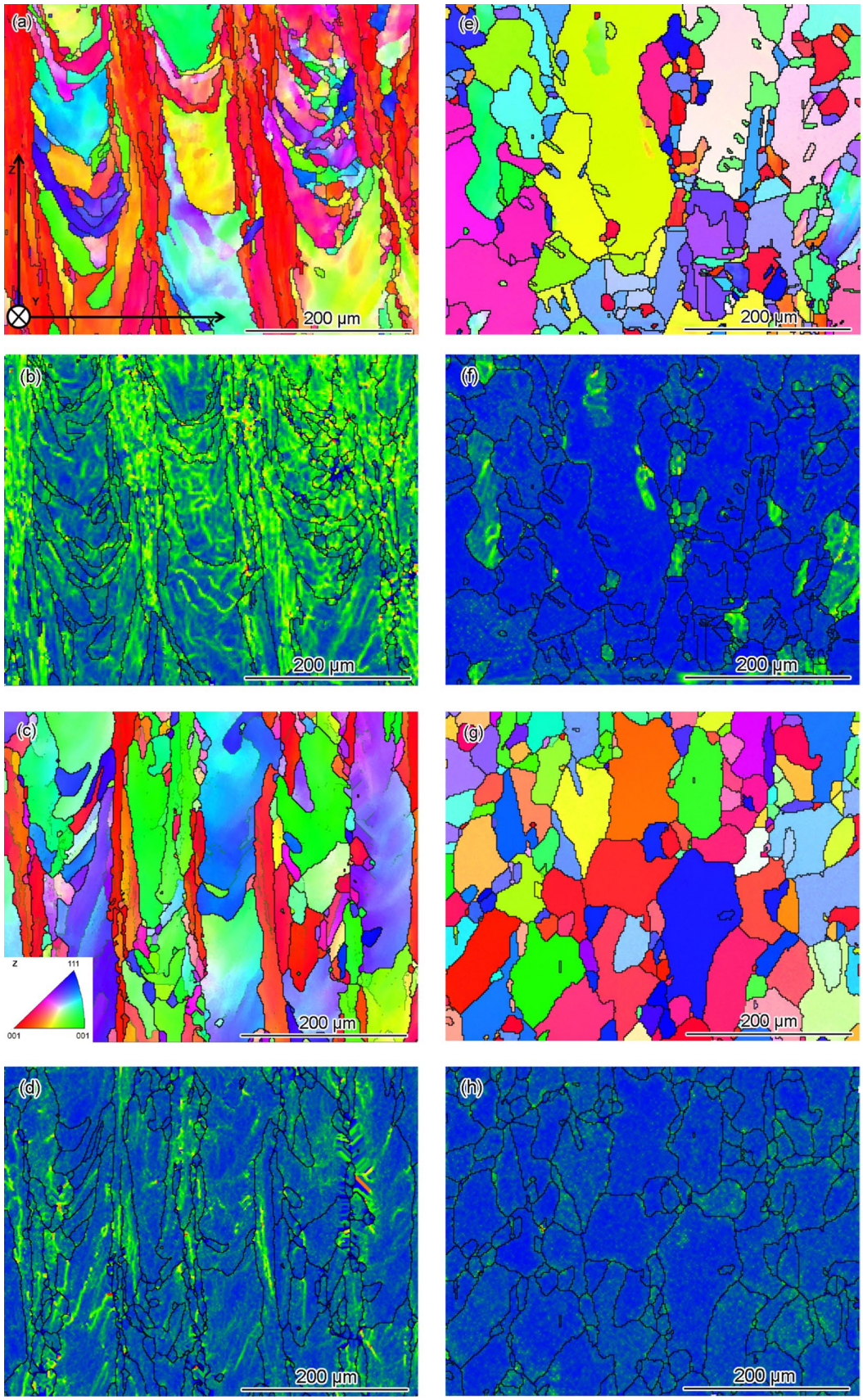
(a)
Z
Y
X
200 μm
(e)
200 μm
(b)
200 μm
(f)
200 μm
(c)
Z
111
001
001
200 μm
(g)
200 μm
(d)
200 μm
(h)
200 μm

◂**Fig. 14** EBSD orientation image maps and local misorientation maps of the SLM FGH4096M after HT: **a**, **b** DA, the inset is sample coordinate; **c**, **d** SSA(1050 ℃); the inset is the inverse pole figure; **e**, **f** SSA(1130 ℃); **g, h** DSSA(1170 ℃ + 1050 ℃)

tertiary γ′ precipitates played an important role in improving the mechanical properties of the alloys. But this conclusion differed from the view proposed in references [17] and [31], in which there were three sizes of γ′ precipitates in the nickel-based PM superalloys with the best comprehensive properties.

4 Discussion

Compared with the SLM alloy, the grain morphology of the SLM + DA alloy did not change significantly. The changing colors in each grain reveal the orientation gradient and a large number of small angle boundaries in each grain, as shown in Fig. 14a. Meanwhile, it can be inferred from Fig. 14a, b that the higher strain and stored energy exist in the alloy. However, a large number of nano-sized γ′ precipitates were formed in the SLM + DA alloy, which was the main factor affecting the performance of the alloy. Since the SLM alloy with a high cooling rate was in a supersaturated state, the γ′ strengthening precipitates were uniformly and densely dispersed inside the alloy during the DA process. It was obviously for this reason that the internal dislocation slip paths were greatly reduced and the external force required for the dislocation slip was increased, resulting in the increase of the yield strength. A large number of γ′ precipitates further increased the ultimate strength and hardness of the alloy. However, the elongation of the alloy decreased due to the reduction of dislocation slip passages, which made dislocations hard to slip.

Similarly, a large number of γ′ precipitates in the SLM + SSA (1050 ℃) alloy enhanced the strength of the alloy, compared with the SLM alloy. The alloys maintained the columnar grains with different orientations, as shown in Fig. 14c. However, compared with the SLM + DA alloy, the SLM + SSA (1050 ℃) alloy indicated lower strength, but higher elongation. The effects of DA and SSA (1050 ℃) on the microstructure of the SLM alloy were concerned: (1) In solution treatment, the recovery process of the SLM alloy occurred at a higher temperature than that in aging treatment, and the number of dislocations in the alloy decreased. In this case, some of the stresses would be released, which was shown in Fig. 14d. (2) Some of the γ′ precipitates segregated at the boundaries of the grain, dendritic structure and cellular structure under solution temperature of 1050 ℃, consuming the strengthening elements dissolving in the alloy. Therefore, the precipitation of tertiary γ′ phase was not uniform and dense during the subsequent aging process, the amount of γ′ phase precipitation was reduced, and the dislocation slip paths were increased. As a result, the strength of the SLM + SSA (1050 ℃) alloy was higher than the SLM alloy, lower than the SLM + DA alloy, and the elongation of the SLM + SSA (1050 ℃) alloy was higher than the SLM + DA alloy.

The microstructure of the SLM alloy changed greatly after the SSA (1130 ℃) treatment. As the solution temperature reached the recrystallization temperature of the alloy, the grain boundaries of the SLM alloy with high storage energy migrated rapidly and the grains began to recrystallize and develop towards equiaxed grains, as shown in Fig. 14e. At the same time, as the solution temperature reached the fully dissolving temperature of the γ′ phase, the γ′ phase and the strengthening elements were dissolved in the matrix, so the alloy was in a supersaturated state and the strengthening elements were uniformly distributed in the matrix. During the aging process, the strengthening precipitates were uniformly and compactly formed inside the grains in the form of tertiary γ′ phase, of which the morphology was similar to that in the SLM + DA alloy. The main differences in grain morphology between the SLM + DA and SLM + SSA (1130 ℃) alloys were as follows: (1) The columnar grains of the SLM alloy were still retained after DA, while the grains in the SLM + SSA (1130 ℃) alloy showed irregular shapes, and tended to be equiaxed. (2) During solid solution treatment, because of the occurrence of recovery and recrystallization, most of stress and a large number of defects, dendritic structures and equiaxed structures disappeared in the alloy, which could be deduced by the Fig. 14f. By comparing the properties between the SLM + DA and SLM + SSA (1130 ℃) alloys, it could be concluded that the dendritic structures and equiaxed structures in columnar grains improved the strength of the alloy to some extent. The occurrence of recovery and recrystallization process reduced the number of dislocations and made the alloy in a low energy state. During the tensile process of the SLM + SSA (1130 ℃), the dislocations began to increase due to the external force, which improved the elongation of the alloy.

The metallographic microstructure and the precipitate morphology of the SLM + DSSA (1170 ℃ + 1050 ℃) alloy were very different from those of the SLM alloy. After the first solid solution treatment at 1170 ℃, the alloy recovered and recrystallized, the dendritic structures and equiaxed structures disappeared, and the grains tended to be equiaxed in irregular shapes. Meanwhile, the strengthening elements were dissolved in the matrix and the alloy was in a supersaturated state at the temperature exceeding the full dissolution temperature of γ′ phase. When the alloy underwent the second solid solution treatment at 1050 ℃, the γ′ phase began to precipitate from the supersaturated matrix. Firstly the primary γ′ phase precipitated at the grain boundary, the secondary γ′ phase nucleated and grew in the grain

at the middle and later stages of the second solid solution, and the larger tertiary γ′ phase began to nucleate at the later stage. During the subsequent aging treatment, the primary and secondary γ′ precipitates continued growing, and the tertiary γ′ precipitates were formed and grew. Compared with the SLM + SSA (1130 ℃) alloy, the differences between them were as follows: (1) There were three sizes of γ′ precipitates in the SLM + DSSA (1170 ℃ + 1050 ℃) alloy. The primary γ′ precipitates were mainly distributed at the grain boundary, the secondary γ′ precipitates were mainly distributed in the grain, and the tertiary γ′ precipitates were in two sizes and in various shapes. (2) The γ′ precipitates in the SLM + DSSA (1170 ℃ + 1050 ℃) alloy grew up by absorbing strengthening elements or combining with each other. In this case, the high contents of Al and Ti in the γ′ phase would lead to the increase of lattice distortion and strain energy between γ′ phase and matrix, which could be inferred from the existence of partially splitting γ′ phase in the alloy. Compared with the room temperature tensile properties of the SLM + SSA (1130 ℃) alloy, the strength of the SLM + DSSA (1170 ℃ + 1050 ℃) alloy increased, but the elongation decreased. While the γ′ precipitates with different sizes increased the slip paths of dislocations, the morphology of γ′ precipitates with different sizes in the alloy varied greatly, and the contents of Al and Ti in the γ′ phase were high, which led to the increase of lattice distortion between the γ′ phase and the matrix. Thus the dislocation slip resistance would be enhanced, thereby increasing the strength and reducing the elongation of the alloy.

The microstructural differences between the SLM + DSSA (1170 ℃ + 1050 ℃) and SLM + SSA (1050 ℃) alloys were obvious: (1) The grains in the SLM + DSSA (1170 ℃ + 1050 ℃) alloy were irregular and tended to be equiaxed as shown in Fig. 14g, while the SLM + SSA (1050 ℃) alloy maintained dendritic structures and equiaxed structures within columnar grains. (2) The lattice distortion between the γ′ phase and the matrix in the SLM + DSSA (1170 ℃ + 1050 ℃) alloy was larger than that in the SLM + SSA (1050 ℃) alloy, which can be inferred from the uniform and lesser stress in the Fig. 14h. However, the γ′ precipitates in the SLM + SSA (1050 ℃) alloys did not indicate too many combination phenomena, and only the γ′ precipitates at the grain boundary tended to combine with each other. By comparing the properties of the SLM + DSSA (1170 ℃ + 1050 ℃) and SLM + SSA(1050 ℃) alloys, it could be inferred that the lattice distortion between the γ′ phase and the matrix could play a positive role in improving the strength of the alloy. The yield strength of the SLM + DSSA (1170 + 1050 ℃) alloy was similar to that of the SLM + SSA (1050 ℃) alloy, but the ultimate strength of the SLM + DSSA (1170 + 1050 ℃) alloy is higher than that of the SLM + SSA (1050 ℃) alloy, which is mainly due to the relatively concentrated stress caused by the tangle of dislocations in the SLM + SSA (1050 ℃) alloy at the later stage of tensile. By comparing the elongation of the two alloys, it could be seen that the morphology of the γ′ phase had a great impact on the elongation of the alloys.

From Fig. 14a, c, e, g, it can be observed that the occurrence of recrystallization after HT can reduce the texture to some extent and reduce the effect of anisotropy on the alloy, which has been proved by the random distribution of grain orientations. The stress in the alloy would be released during HT, as shown in Fig. 14b, d, f, h, because of the occurrence of recovery and recrystallization. The higher the temperature, the more sufficient the stress release. Figure 15 shows that the local misorientation angle decreases with the increase of solution temperature, which indicates more stress release at a higher solution temperature.

Figure 16 shows the relationship between the average size of γ′ precipitate and the strength of the alloys under different HTs. The size of γ′ precipitate in the SSA (1130 ℃) alloy is similar as that in the DA alloy, but the latter exhibits much higher strength. The SSA (1050 ℃) and DSSA (1170 ℃ + 1050 ℃) alloys with larger sized γ′ precipitates exhibit similar strength to the SSA (1130 ℃) alloy. This indicates that the size of γ′ precipitate is not the only factor affecting the strength, which may also be strongly related to the number and the distribution of γ′ precipitate, grain morphology and so on.

Generally speaking, the occurrence of recovery and recrystallization can improve the plasticity by releasing residual energy and refining grains in the alloy. For example, there were much higher degrees of recovery and recrystallization in the SSA and DSSA alloys, all of which owned much higher plasticity than the DA alloy. However, those heat treatments also resulted in a large quantity of strengthening precipitates in the alloys, which did harm to the plasticity by reducing dislocation slip passages. Although the

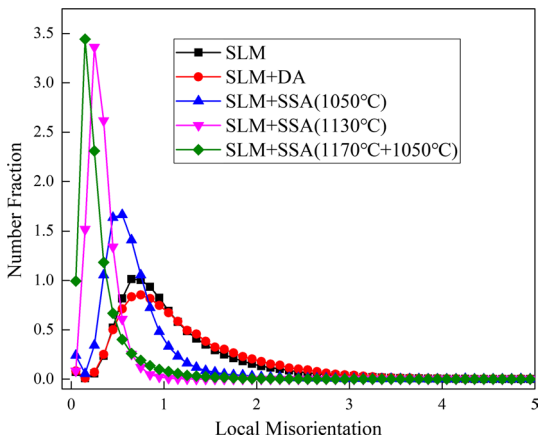

Fig. 15 Local misorientation angles of SLM FGH4096M under different heat treatments

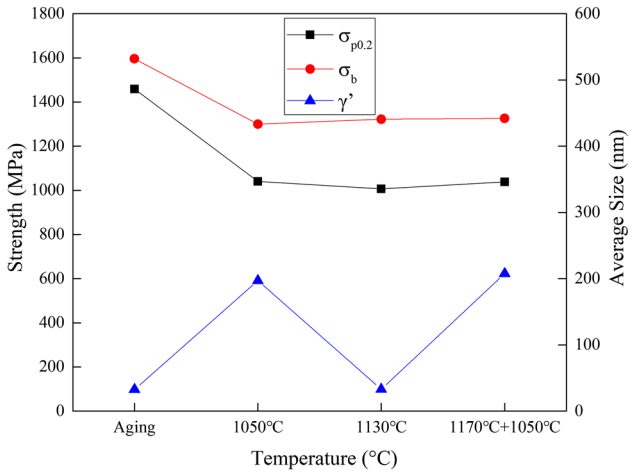

Fig. 16 The relationships between the average size of γ′ and strength of SLM FGH4096M under different heat treatments

SLM alloy owned much higher residual energy, it exhibits much higher plasticity than the other SLM + HT alloys. A reasonable explanation of this result may be that during the heat treatments, the adverse effect of precipitation strengthening on the plasticity greatly surpassed the beneficial effect of recovery and recrystallization on the plasticity.

5 Conclusions

1. The alloys under SLM + DA and SLM + SSA with solution temperature below 1090 ℃ retained the similar grain morphology as the SLM alloy owned. When the solution temperature was above 1100 ℃ for the SLM + SSA alloy, reaching the temperature of recovery and recrystallization, the columnar grains as well as the dendritic structure and equiaxed structure within the grains disappeared, and the grains tended to be equiaxed. The microstructure tended to be isotropic with the number of equiaxed grains increasing.
2. During the DA treatment and SSA treatment at solution temperature above 1110 ℃, the tertiary γ′ precipitates were dispersed more uniformly in the alloy. When the solution temperature ranged from 1010 to 1090 ℃, the secondary γ′ precipitates in the SLM + SSA alloy were distributed along the growth direction of the dendritic structure. With the increase of temperature, the number and the arrangement regularity of the secondary γ′ precipitates decreased gradually.
3. When the SLM alloy was treated by DSSA (1170 ℃ + 1050 ℃), there were three sizes of γ′ precipitates in the alloy. The γ′ precipitates with larger size began to grow in the way of absorbing smaller sized γ′ precipitates, and the γ′ precipitates with similar size grew in the way of combining with each other. The lattice distortion between secondary γ′ phase and γ matrix increased after the DSSA treatment.
4. The large number, uniform size and dense distribution of γ′ precipitates were beneficial to the improvement of the tensile strength and hardness of the alloy, at the expense of the elongation. The larger the distortion between γ′ phase and matrix, the higher the strength and hardness of the alloy. But the excessive distortion could lead to the instability of γ′ precipitates[35].
5. During the heat treatments, the formation of strengthening precipitates and the recovery and recrystallization process usually occurred simultaneously in the alloys. The former could enhance the strength but reduce the plasticity, while the latter was beneficial to the plasticity. Therefore, all the SLM + HT alloys exhibited much higher strength than the SLM alloys. The SLM + SSA and SLM + DSSA alloys owned higher degree of recovery and recrystallization, thus leading to higher plasticity than the DA alloy. However, for all the SLM + HT alloys, the adverse effect of precipitation strengthening on the plasticity seemed to greatly overtake the beneficial effect of recovery and recrystallization on the plasticity. Therefore, all the SLM + HT alloys exhibited much lower plasticity than the SLM alloy in the present work.

Acknowledgements The authors thank the Director Zhang Guo-Wei and Zhang Guo-Dong of Hangxing Lihuan Technology Co., Ltd, and the Director Ye Jun-Qing of Guizhou Anda Aviation Forging Co., Ltd for their valuable contributions. The work was supported by Shenzhen Science and Technology Innovation Commission under projects (No. JSGG20180508152608855 and No. JCYJ20170817110358927).

References

1. C. Jia, C. Ge, Q. Yan, Mater. Sci. Eng. A **659**, 287 (2016)
2. Z. Huda, P. Edi, Mater. Des. **46**, 552 (2013)
3. P. Xing, Y. Zhang, J. Jia, Trans. Mater. Heat Treat. **39**, 88 (2018). **(in chinese)**
4. O. Senkov, D. Mahaffey, S. Semiatin, C. Woodward, Metall. Mater. Trans. A **45**, 5545 (2014)
5. L. Tan, G. He, F. Liu, Y. Li, L. Jiang, Material **328**, 1 (2018)
6. T. Brynk, Z. Pakiela, K. Ludwichowska, B. Romelczyk, R. Molak, M. Plocinska, J. Kurzac, T. Kurzynowski, E. Chlebus, Mater. Sci. Eng. A **698**, 289 (2017)
7. N. Nadammal, S. Cabeza, T. Mishurova, T. Thiede, A. Kromm, C. Seyfert, L. Farahbod, C. Haberland, J. Schneider, P. Portella, G. Bruno, Mater. Des. **134**, 139 (2017)
8. W. Tillmanna, C. Schaaka, J. Nellesen, M. Schaper, M.E. Aydinöz, K.P. Hoyer, Addit. Manuf. **13**, 93 (2017)
9. Z.M. Wang, K. Guan, M. Gao, X.Y. Li, X.F. Chen, X.Y. Zeng, J. Alloys Compd. **513**, 518 (2012)
10. S. Holland, X. Wang, J. Chen, W. Cai, F. Yan, L. Li, J. Alloys Compd. **784**, 182 (2019)

11. V.D. Divya, R. Muñoz-Moreno, O.M.D.M. Messé, J.S. Barnard, S. Baker, T. Illston, H.J. Stone, Mater. Charact. **114**, 62 (2016)
12. X. Yao, S.K. Moon, B.Y. Lee, G. Bi, Int. J. Precis. Eng. Manuf. **18**, 1693 (2017)
13. X. Li, J.J. Shi, G.H. Cao, A.M. Russell, Z.J. Zhou, C.P. Li, G. F. Chen, Mater. Des., 180, 107915 (2019)
14. F.E. Zhang, L. Levine, A.J. Allen, R.M. Stoudt, G. Lindwall, A.E. Lass, E.M. Williams, Y. Idell, E.C. Campbel, Acta Mater. **152**, 200 (2018)
15. W. Huang, H. Yu, J. Yin, Z. Wang, X. Zeng, Acta. Metall. Sin. **52**, 1089 (2016). **(in chinese)**
16. Cademic Committee of the Superalloy CMS (2012) *China Superalloys Handbook*, Standards Press of China, Beijing, pp. 635–636. **(in chinese)**
17. J.T. Guo (2008) *Materials Science and Engineering for Superalloys*, Science Press, Beijing, pp. 658–669. **(in chinese)**
18. M. Li, J. Coakley, D. Isheim, G. Tian, B. Shollock, J. Alloys Compd. **732**, 765 (2018)
19. Z. Peng, G. Tian, J. Jiang, M. Li, Y. Chen, J. Zou, F. Dunne, Mater. Sci. Eng. A **676**, 441 (2016)
20. F. Geiger, K. Kunze, T. Etter, Mater. Sci. Eng. A **661**, 240 (2016)
21. Z. Hao, T. Tian, X. Li, Q. Yan, C. Ge, Y. Yan (2019) Chin. J. Rare Met. https://doi.org/10.13373/j.cnki.cjrm.XY18120020. (in chinese)
22. E. Chlebus, K. Gruber, K. Kuźnicka, J. Kurzac, T. Kurzynowski, Mater. Sci. Eng. A **639**, 647 (2015)
23. O. Messé, R. Muñoz-Moreno, T. Illston, S. Baker, H. Stone, Addit. Manuf. **22**, 394 (2018)
24. R. Muñoz-Moreno, V. Divya, O. Messé, T. Illston, S. Baker, H. Stone, Effect of heat treatments on the microstructure and texture of CM247LC processed by selective laser melting, in *Proceedings of the 13th International Symposium on Superalloys.* (TMS, New York, 2016), pp. 375–382.
25. R. Fu, F.L. Li, F.J. Yin, D. Feng, Z.L. Tian, L.T. Chang, Mater. Sci. Eng. A **638**, 152 (2015)
26. Y.Q. Ning, M.W. Fu, W. Yao, Mater. Sci. Eng. A **539**, 101 (2012)
27. K.N. Amato, S.M. Gaytan, L.E. Murr, E. Martinez, P.W. Shindo, J. Hernandez, S. Collins, F. Medina, Acta Mater. **60**, 2229 (2012)
28. C. Jia, F. Zhang, K. Wei, S. Lv, J. Alloys Compd. **770**, 166 (2019)
29. C. Jia, Y. Li, F. Zhang, S. Lv, Met. Powder Rep. **73**, 94 (2018)
30. J.A. Gonzalez, J. Mireles, S.W. Stafford, M.A. Perez, C.A. Terrazas, R.B. Wicker, J. Mater. Process. Tech. **264**, 200 (2019)
31. C. Jia, F. Zhang, Y. Li, S. Lv, C. Ge, Met. Powder Rep. **73**, 319 (2018)
32. P. Kanagarajah, F. Brenne, T. Niendorf, H.J. Maier, Mater. Sci. Eng. A **588**, 188 (2013)
33. D. Tomus, Y. Tian, P.A. Rometsch, M. Heilmaier, X.H. Wu, Mater. Sci. Eng. A **667**, 42 (2016)
34. B.F. Hu, G.Q. Liu, K. Wu, G.F. Tian, Acta. Metall. Sin. **48**, 257 (2012). **(in chinese)**
35. T.T. Wang, C.C. Ge, C.L. Jia, J. Wang, T.F. Gu, Acta Phys. Sin. **64**, 1 (2015). **(in chinese)**